Radial thermo-chemical structure beneath Western and Northern Pacific from seismic waveform inversion

Supplementary material

Frédéric Deschamps[1,a], Kensuke Konishi[1], and Nobuaki Fuji[2], and Laura J. Cobden[3]

[1] Institute of Earth Sciences, Academia Sinica, 128 Academia Road, 11529 Taipei, Taiwan
[2] Institut de Physique du Globe de Paris, 1 rue Jussieu, 75238 Paris cedex 05, France
[3] Department of Earth Sciences, Utrecht University, Heidelberglaan 8a 3584 CB, Utrecht, The Netherlands

[a] Corresponding author. Email: frederic@earth.sinica.edu.tw

This supplementary material contains details on the methods used to invert waveform data for 1-D radial models of shear-wave velocity anomalies ($dlnV_S$) and quality factor (Q_S), details on the modelling of the effect of post-perovskite on shear-wave speed anomalies, on the estimation of the activation enthalpy of attenuation, and on the construction of radial thermo-chemical models, Supplementary Tables S1 and S2, listing the seismic events used to build the radial models of shear-wave speed and seismic quality factor, and Supplementary Figures S1 to S10.

Methods

Inversion for radial models of shear-wave velocity anomalies and quality factor

The full-waveform inversion used to obtain 1-D radial models of shear-wave velocity anomalies ($dlnV_S$) and quality factor (Q_S) was described in detail in Konishi et al. (2017). Important points are summarised in the main text and below.

Static corrections. To remove near-source and near-receiver effects due to local structures in the crust or shallow mantle, we performed static corrections. Assuming that S and ScS waves travel along the same path at depths shallower than about 2000 km, *i.e.*, they are similarly affected by shallow structures, we cancel these effects by normalizing the observed and synthetic waveforms with respect to the amplitude of the direct S-wave arrival of each source-receiver pair, and by aligning these arrivals so that waveform inversion measures the differential traveltimes of ScS phases. We also calculated the difference between the observed

S-wave arrival and that predicted by PREM, and found that these difference are evenly distributed around zero and do not show correlation between variability and path location. This suggests that the crust and shallow mantle along the receiver regions are close to PREM and fairly homogeneous.

One may point out that for the epicentral distances of our datasets, in particular at Western Pacific (WP), the assumption that seismic rays follow similar paths in the transition zone is not entirely valid, and that models of seismic structure based on travel time data may then be substantially biased. Here, however, we used waveform data, and the methodology we developed allows us to separate the effects of the transition zone from those of deeper regions. More precisely, the kernels of waveforms (instead of that of traveltimes or amplitudes) for the transition zone and for the lowermost mantle are orthogonal, as was demonstrated by Konishi et al. (2014), who used a dataset similar to our WP dataset (see their Figure 19).

Source-time functions. To build source-time functions, we pick *S*-wave peaks (up-down) in all the observed and synthetic waveforms, normalize waveform with peak amplitude, and stack these normalized waveforms by the centre time of the *S*-wave peaks. We then transfer the stacked waveforms to the frequency domain using a classical Fourier-transform. Source-time functions are finally computed simply by dividing the observed and synthetic stacked waveforms in the frequency domain. Konishi et al. (2017) assessed the validity of these source-time functions by computing synthetic waveforms with source-time functions taken from the SCARDEC catalogue (Vallée et al., 2011), and by comparing these waveforms with the synthetics used in this study. Small differences appear, but they do not affect our results because the frequency range we used samples relatively low frequencies. If extended to higher frequencies, however, a careful investigation may be required.

Regional trends. Prior to inversion, we determined regional trends in amplitude and traveltime anomalies by comparing synthetic peak amplitude and traveltime of *S* and *ScS* phases with real data. For this, we first automatically pick the negative and positive peaks of both *S* and *ScS* wavelets independently. We then define the traveltime as the midpoint time of the negative and positive wavelet peaks, and the amplitude as a difference between the positive and negative peaks. This method is rapid and appropriate for the data set we used, since waveforms filtered up to 0.08 Hz have simple shapes, and the results obtained by handpicking or cross-correlation methods lead to similar values. It is important to note that these peak amplitude and travel-time measurements are used only to determine regional

trends. Radial models, by contrast, are based on full waveform inversions (see below). Discrepancies between observed and synthetic data are estimated by systematically looking at the differences in traveltimes and amplitudes for two seismic phases, *S* and *ScS*. High variability, if correlated with path location, indicates potential lateral structures. The initial dataset may then be split in sub-datasets according to the observed local variations. Supplementary Figure S1 shows traveltime residuals and amplitude ratios at WP and NP plotted along their respective regression lines, *i.e.*, the lines defined by the linear regression of the bounce points of the raypaths (red lines and black crosses in Figure 1) on the CMB (in the case of NP, this line is close to the -175° meridian). At WP, traveltime residuals and amplitude ratios clearly vary along the regression line. Based on this observation, we split the initial dataset into 3 sub-datasets, and inverted each of them for models of dlnV_S and Q_S. The choice of the exact limits between each dataset is subjective. We separated the data set so that the ray paths of the central sub-dataset sample the entire region covered by the Caroline plume. Interestingly, the gradient of both traveltime residuals and amplitude ratios along the regression line is very smooth, suggesting that small differences in the limits between sub-datasets have a limited impact on our output models. To check this point, we performed additional inversions in which we slightly modified the limits between the sub-datasets, but did not find significant changes in the output 1-D models of V_S and Q_S. For NP, the whole dataset is homogeneous, *i.e.* we did not find substantial variations in traveltime and waveform anomalies. We thus inverted this data set as a whole.

Waveform inversion. To obtain profiles of V_S and Q_S, we perform a full waveform inversion. This inversion is designed to minimize the difference (measured with L2-norm) between observed and synthetic displacements U at each time t. Assuming that displacement is affected by perturbations in both shear modulus (or rigidity) μ and attenuation q, from which the quality factor $Q_S = 1/q$ is defined, the difference in displacement is given by

$$\delta U = \frac{\partial U}{\partial \mu}\delta \mu + \frac{\partial U}{\partial q}\delta q. \tag{S1}$$

Following Fuji et al. (2010), the frequency dependences of rigidity and its perturbation are

$$\mu(\omega) = \mu_0 \left[1 + \frac{2q}{\pi}\ln(\omega/\omega_0)\right](1 + iq) \tag{S2}$$

and $\delta\mu(\omega) = \left[1 + \frac{2q}{\pi}\ln\left(\frac{\omega}{\omega_0}\right)\right](1 + iq)\delta\mu_0 + \mu_0\left[\frac{2}{\pi}\ln\left(\frac{\omega}{\omega_0}\right) + i\left(1 + \frac{4q}{\pi}\ln\left(\frac{\omega}{\omega_0}\right)\right)\right]\delta q,$ (S3)

where μ_0 is the value of the rigidity at a reference frequency ω_0, which we fixed to 1 Hz in our inversions. The partial derivative of the displacement with respect to rigidity is detailed in

Geller and Hara (1993) and Fuji et al. (2010) and can be used to derive the partial derivative with respect to attenuation, $\partial U / \partial q = \partial U / \partial \mu \times \partial \mu / \partial q$, where

$$\frac{\partial \mu}{\partial q} = \mu_0 \left[\frac{2}{\pi} \ln \left(\frac{\omega}{\omega_0} \right) + i \left(1 + \frac{4q}{\pi} \ln \left(\frac{\omega}{\omega_0} \right) \right) \right]. \tag{S4}$$

These derivatives are used to build the inverse matrix **A** of the linearized problem (see main text and Eq. (1)).

The inverse matrix is further used to calculate the sensitivity kernels, which are defined as the diagonal of the Hessian matrix $\mathbf{A}^T\mathbf{A}$. These kernels are built for PREM and are plotted on Supplementary Figure S2 for both WP (green curves) and NP (red curves). Generally speaking, because we use *ScS* phases, the shallower the depth, the weaker the sensitivity. Detailed changes in sensitivity, however, depend on the detailed geometry of each dataset and on the path coverage. In addition, changes in waveforms are more complex and less intuitive to predict than changes in travel times. For instance, at WP sensitivity regularly decreases with altitude above the CMB, as expected, while at NP, it varies more irregularly. In particular, sensitivity at NP is very low in the depth range 2550-2700 km. The origin of this low sensitivity layer is not clear. Possible causes include the depth distribution of earthquakes, and an unequal distribution of raypaths as a function of epicentral distance, with number of raypaths sampling this depth range being small compared to raypaths sampling shallower and deeper ranges. Importantly, at depths greater than 2700 km, sensitivities are large at both WP and NP, *i.e.*, our models provides a good sampling of the lowermost mantle in these regions.

To assess the resolution of our models, we performed checkerboard tests (see main text and Figure 4). These synthetic tests are free of noise, *i.e.*, they correspond to the best possible case. However, it is important to note that Konishi et al. (2014) showed that the inversion results are robust with at least white noises. It is also important to note that the inter-dependency between the model parameters in our sensitivity kernels is limited, as indicated by our checkerboard tests.

Post-perovskite fraction as a function of temperature

The post-perovskite (pPv) phase is a high pressure phase of bridgmanite that is expected to be locally present in the deep mantle (Cobden et al., 2015). If so, lateral variations in its stability field may contribute to the observed shear-wave speed anomalies (dlnV_S). The stability field of pPv depends both on temperature and pressure, and the exact values of the transition temperature and pressure further depend on the mineralogical composition. Based on a recent

compilation of all available experimental and *ab initio* data (Cobden et al., 2015), we fixed the temperature of the transition at $z = 2850$ km to $T_{pPv} = 3150$ K. To evaluate the effect of pPv on the values of $dlnV_S$ observed at a given location, one needs to estimate the fraction of pPv at this location, X_{pPv}, and the reference (horizontally averaged) fraction of pPv, $X_{pPv,ref}$, as a function of the local and reference temperature, T and T_{ref}.

Here, we defined the reference fraction of pPv such that it decreases linearly from 1 to 0 for reference (horizontally averaged) temperature T_{ref} between temperatures $T_{low} = (T_{pPv} - dT_{max})$ and $T_{up} = (T_{pPv} + dT_{max})$, where dT_{max} is the maximum amplitude of temperature variations and is typically around 500 K in the deep mantle (Trampert et al., 2004; Mosca et al., 2012). This leads to

$$X_{pPv,ref} = \begin{cases} 1 \ \ if \ T_{ref} \leq T_{low} \\ \frac{1}{2}\left[1 - \frac{(T_{ref}-T_{pPv})}{dT_{max}}\right] \ \ if \ T_{low} \leq T_{ref} \leq T_{up} \\ 0 \ if \ T_{ref} \geq T_{up} \end{cases} \tag{S5}$$

This definition implicitly assumes that mantle temperature at a given depth is distributed as a boxcar function between $T_{min} = (T_{ref} - dT_{max})$ and $T_{max} = (T_{ref} + dT_{max})$. The volume fraction of mantle where pPv is stable at this specific depth is then given by the volume fraction where temperature is between T_{min} and T_{pPv} (Figure S6). This fraction is equal to zero if $T_{min} > T_{pPv}$, and to one if $T_{max} < T_{pPv}$. Taking $T_{ref} = 3500$ K, $dT_{max} = 500$ K, and $T_{pPv} = 3150$ K, $X_{pPv,ref}$ is equal to 0.15. This value is much lower than that estimated from probabilistic tomography (Mosca et al., 2012), around 0.7. This disagreement is however related to differences in the assumed value of T_{ref}, which is around 3000 K in Mosca et al. (2012). Fixing $T_{ref} = 3000$ K in Eq. (S5) leads to $X_{pPv,ref} = 0.65$, now in good agreement with Mosca et al. (2012). The definition of $X_{pPv,ref}$ given by Eq. (S5) further indicates that for $T_{ref} \geq 3650$ K, $X_{pPv,ref} = 0$, *i.e.*, the CMB region is free of pPv.

The stability field of pPv depends on the distribution of temperature. The estimated temperature at a specific location is an average temperature over the volume of the cell defined by the radial and lateral parameterizations of the model. The fraction of pPv may thus vary within this volume. In addition, bridgmanite does not entirely transform to pPv exactly at temperature T_{pPv}. Instead, transformation occurs over a narrow range of temperature, or thermal width. It is thus meaningful to define a fraction of pPv (between 0 and 1) at a given point of the model. Here, we define the fraction of pPv at local temperature T with

$$X_{pPv} = \frac{1}{2}\left[1 - \tanh\left(\frac{T-T_{pPv}}{\delta T_{pPv}}\right)\right], \tag{S6}$$

5

where T_{pPv} is, again, the temperature of the transition to pPv, which we fixed to $T_{pPv} = 3150$ K at $z = 2850$ km, and δT_{pPv} is a typical temperature anomaly, modeling the thermal width of the transition from bridgmanite to pPv and the temperature variation within the volume considered. Here, we fixed δT_{pPv} to 20 K. With these definitions and values of T_{pPv} and δT_{pPv}, the fraction of pPv is equal to one up to temperature equal to 3100 K, goes to zero for temperature larger than 3200 K, and varies almost linearly between these two points.

The anomaly in pPv at a given location, dX_{pPv}, is then simply given by the difference between the local (Eq. S6) and horizontally averaged (Eq. S5) fractions of pPv, $dX_{pPv} = X_{pPv} - X_{pPv,ref}$. Because the local temperature is given by $T = dT_{VS} + T_{ref}$, the local fraction of pPv, X_{pPv}, and thus dX_{pPv} implicitly depend on dT_{VS}. Houser (2007) did a first attempt to parameterize these dependences by estimating the thickness of pPv layer above the CMB as a function of the temperature anomaly, and calculating *a posteriori* the contribution of this pPv layer to the observed $d\ln V_S$. Following this method, and for a temperature anomaly of 800 K compared to the absolute minimum temperature, the value of $d\ln V_S$ accounting for the presence of pPv is lower by about 1.5 % than the purely thermal one. Here, we explicitly accounted for this dependence in the expression of the temperature anomaly estimated from $d\ln V_S$. Replacing dX_{pPv} in Eq. (2) of main text by its expression as a function of dT_{VS}, leads to

$$dT_{VS} = \frac{(d\ln V_S - S_{Fe}dx_{Fe})}{S_T} - \frac{S_{pPv}}{2S_T}\left[1 - \tanh\left(\frac{T_{ref} + dT_{VS} - T_{pPv}}{\delta T_{pPv}}\right)\right]. \tag{S7}$$

Equation (S7) must then be solved for dT_{VS}. To do this, we used a classical Newton-Raphson zero search method.

Knowledge of the temperature anomaly dT_{VS} at a given location further gives access to the fraction of pPv at this location (Eq. S6), and to its anomaly dX_{pPv} with respect to the reference fraction $X_{pPv,ref}$ (Eq. S5). Figure S7 shows dX_{pPv} at WP (*i.e.*, with $d\ln V_S$ = -2.5 %) as a function of the reference temperature, and assuming two possible origins for the observed $d\ln V_S$, purely thermal or thermo-chemical with an enrichment in iron of 3.5 % at WP. Several trends can be identified, depending on T_{ref}. First, for $T_{ref} \geq 3650$ K, the whole CMB region is free of pPv, and obviously both $X_{pPv,ref}$ and dX_{pPv} are equal to 0. As T_{ref} decreases, pPv is locally stable and $X_{pPv,ref}$ increases. If the temperature at WP, given by $T_{WP} = T_{ref} + dT_{VS}$, is too large, pPv is not stable at this location, *i.e.*, $X_{pPv} = 0$. As a consequence, dX_{pPv} is strictly equal to the opposite of $X_{pPv,ref}$ and its error bar is zero. As T_{ref} continues to decrease, the temperature at WP becomes low enough (within its error bar) for pPv to be stable, and the difference between the local and reference fractions of pPv decreases again. This occurs for

T_{ref} around 3000 K in the purely thermal case, and 3250 K if WP is chemically enriched in iron by 3.5 %.

Activation enthalpy of attenuation

The determination of temperature anomalies from quality factor (dT_Q, Eq. 6) requires the knowledge of the activation enthalpy H of attenuation at lower mantle conditions. Activation enthalpy increases with depth (pressure) following $H = E + pV$, where E is activation energy, V activation volume, and p the pressure.

Activation energy for the lower mantle minerals, bridgmanite and ferropericlase have been measured experimentaly (for a short review, see Matas and Bukowinski, 2007). For ferropericlase, it has been found between about 230 kJ/mol (Getting et al., 1997; Yamazaki and Irifune, 2003) and 253 ± 50 kJ/mol (Holzapfel et al., 2003). Yamazaki and Irifune (2003) noted that it may strongly vary with the iron content, from values as low as 113 ± 74 kJ/mol for FeO, to 226 ± 32 for MgO. For bridgmanite, and at 25 GPa, Yamazaki et al. (2000) found 336 kJ/mol and 311 kJ/mol for lattice and grain boundary diffusions, respectively, which, assuming $V = 1.2 \times 10^{-6}$ m^3/mol (see below) leads to 306 kJ/mol and 291 kJ/mol. At similar pressures (22 to 26 GPa), Holzapfel et al. (2005) found slightly higher values, at 414 ± 62 kJ/mol, *i.e.* about 385 kJ/mol at ambient pressure. Defining the activation energy of an aggregate by the harmonic average of the activation energies of each mineral that constitute this aggregate, and taking $E_{Bm} = 306$ kJ/mol and $E_{Fp} = 223$ kJ/mol, one gets an activation energy $E = 286$ kJ/mol for an aggregate composed of 80% bridgmanite and 20 % ferropericlase. This is also the value used by Dannberg et al. (2017) and Lau and Faul (2019). With Holzapfel et al. (2003, 2005) data, one gets about 350 kJ/mol. The higher bound of E assumed by Dannberg et al. (2017) and Lau and Faul (2019) is slightly higher, $E = 375$ kJ/mol, a value that they derive from Burgers model fit to olivine of Jackson and Faul (2010).

Few experimental data are available for the activation volume V, and most estimates result from modelling or comparison with seismic data and models. Matas and Bukowinski (2007) modelled V from thermo-elastic dataset and the mantle geotherm and found values in the range 0.6×10^{-6}-1.1×10^{-6} m^3/mol for bridgmanite, and between 0.8×10^{-6} and 1.2×10^{-6} m^3/mol for ferropericlase. More recently, Dannberg et al. (2017) developed an anelastic model that accounts for grain size evolution, and performed a grid search to identify the parameter values of their model that explain observed radial profiles of quality factor at best. For activation energy $E = 286$ kJ/mol and frequency exponent $\alpha = 0.274$, the best fitting value of volume activation to the V_S of PREM (Dziewonski and Anderson, 1981) and the Q_S of

QL6 (Durek and Ekström, 1996) is $V = (1.2 \pm 0.1) \times 10^{-6}$ m^3/mol. Using seismic normal modes and tides with periods ranging from 7 min to 18.6 yr, Lau and Faul (2019) found larger values, from about 1.1×10^{-6} to 4.0×10^{-6} m^3/mol, again for $E = 286$ kJ/mol and $\alpha = 0.274$.

Based on these data and modelling, and following Dannberg et al. (2017), we here used $E = 286$ kJ/mol and $V = 1.2 \times 10^{-6}$ m^3/mol to calculate the mean values in dT_Q, and we varied E between 280 and 380 kJ/mol and V between 1.1×10^{-6} and 1.3×10^{-6} m^3/mol to estimate the error bar on dT_Q. This radial model of H is plotted in Figure S10b.

Radial models of temperature and composition

Calculating radial models of temperature anomalies from Q_S (Eq. 6 of main text) requires the definition of depth dependent models of H (Fig. S10a) and T_{ref} (Fig. S10b). Here, T_{ref} is set to 3500 K at the CMB and then decreases adiabatically with altitude following a gradient of 0.3 K/km. To model the thermal boundary layer at the bottom of the mantle, T_{ref} is further assumed to decrease linearly by 500 K between the CMB and an altitude of 200 km ($z = 2680$ km). Because the mantle geotherm is poorly constrained, we imposed an error bar of ±500 K at each depth. Temperature at the CMB thus varies between 3000 and 4000 K, which is usually considered as a robust range (Tackley, 2012). Activation enthalpy depends on pressure p following $H = E + pV$, where E and V are activation energy and volume. As discussed in the previous section, we used $E = 286$ kJ/mol and $V = 1.2 \times 10^{-6}$ m^3/mol to calculate the mean values in dT_Q, and estimated its error bar by varying E between 280 and 380 kJ/mol and V between 1.1×10^{-6} and 1.3×10^{-6} m^3/mol. Finally, based on resolution tests (main text and Figure 4), we imposed an uncertainty of ±15 on the observed model of Q_S.

Estimating temperature anomalies from d$\ln V_S$ (Eq. 2 of main text) requires the prescription of *a priori* radial models of anomalies in iron, dx_{Fe}, and post-perovskite (pPv), dX_{pPv}, at both locations. For Northern profiles (NP), which lies outside the Pacific LLSVP, we assumed that the observed d$\ln V_S$ are purely thermal in origin, *i.e.* d$x_{Fe} = 0$ and d$X_{pPv} = 0$ (the local fraction of pPv is equal to $X_{pPv,ref}$). For Western Pacific profiles, we consider three models: purely thermal models with or without depletion in pPv, and at thermo-chemical model with iron enrichment and depletion in pPv. The radial model of iron anomalies we used (Figure S10c) accounts for expected enrichment in iron in LLSVPs and plumes. From the CMB up to an altitude of 2580 km we fixed dx_{Fe} to 3.5%, consistent with estimates from probabilistic tomography (Trampert et al., 2004; Mosca et al., 2012). From a depth of 2480 km upwards, we set dx_{Fe} to 0.4%, accounting for possible entrainment of dense LLSVP material (Deschamps et al., 2011) by the Caroline plume. The radial model of pPv we

assumed is plotted in Figure S10d. Post-perovskite anomalies are set to -15% in the depth range 2730-2880 km (Fig. S10d). This assumes that, at WP, the Pacific LLSVP is free of pPv, possibly because temperature excess in this region is large enough to prevent pPv from being stable, and that the horizontally averaged fraction of pPv, $X_{pPv,ref}$ is equal to 15%, a value suggested by Eq. (S5) for T_{CMB} = 3500 K (see post-perovskite modelling section). The assumption that the lowermost mantle at WP is free of pPv apparently contradicts the conclusion reached by Cobden et al. (2012), which states that P_{diff} and S_{diff} arrivals are better explained if the Pacific LLSVP is composed of a mixture of bridgmanite and pPv, than if it is free or entirely made of pPv. This study, however, is limited to the spherical harmonic degree 8 structure, and it may not resolve localised regions where pPv would be unstable, for instance because they are too hot. Because it is associated with the Caroline plume, the region we sample at WP could be one such region.

If, as suggested by Mosca et al. (2012), $X_{pPv,ref}$ is larger than the value we assumed, the contribution of pPv anomalies, dX_{pPv}, to the observed $dlnV_S$ would be more important, thus decreasing the dT_{VS} and the importance (and maybe the need) of iron excess to explain these $dlnV_S$. It should be reminded, however, that according to Eq. (6) decreasing T_{ref} would also decrease the temperature anomaly estimated from Q_S, such that estimates of temperature from Q_S and $dlnV_S$ are still incompatible. For instance, taking $X_{pPv,ref}$ = 0.65, which is the value expected for T_{ref} = 3000 K, a $dlnV_S$ of -2.5 % can be explained by a temperature excess of 430 K and a depletion in pPv of 65 %, without the need of an iron excess. In the meantime, taking Q_S = 215, T_{ref} = 3000 K, α = 0.274, and H = 440 kJ/mol, Eq. (6) leads to a temperature excess of 250 K. When uncertainties in Q_S and $dlnV_S$ are taken into account, the values of dT_Q and dT_{VS} obtained for T_{ref} = 3000 K are however consistent (see main article and Figs. 6 and S8).

One may further point out that this radial model of pPv is very simple, since it does not account for the combined effect of the Clapeyron slope and of the depths variations of the reference temperature. This may slightly affect our inferred profile of dT_{VS} but would not alter our conclusions. More specifically, in the depth range 2700-2850 km our simple pPv model overestimates dX_{pPv}, and thus its effect on $dlnV_S$, which further justifies the need for compositional anomalies. Using a more sophisticated radial model, in which dX_{pPv} decreases with altitude according to prescribed Clapeyron slope, would push the estimated dT_{VS} to slightly lower values, improving the agreement between the dT_{VS} calculated assuming an iron excess, and the temperature anomaly estimated from Q (dT_Q) (Figure 8). Finally, experimental data suggested that if enriched in iron, pPv would be stable at shallower depths and larger temperatures compared to magnesium pPv (Mao et al., 2006). It may thus be present within

LLSVPs, if these structures are enriched in iron. For simplicity, we do not consider this possibility. However, if pPv is locally stable at WP, its depletion at this location and the contribution of this depletion to $dlnV_S$ would be, again, smaller. To compensate this, one needs to invoke either larger temperature anomalies, or a chemical source (here, an excess in iron).

Finally, we obtained estimates of error bars in dT_{VS} by accounting for uncertainties in the seismic sensitivities (Figure S5), and in the measured $dlnV_S$. We fixed the latter to $\pm 0.1\%$ based, again, on the resolution tests we performed (Figure 4).

Assuming that Q_S is a good proxy for temperature, it is possible to estimate a radial model of iron anomalies from observed models of $dlnV_S$ and dT_Q following

$$dx_{Fe,inv} = \frac{(dlnV_S - S_T dT_Q - S_{pPv} dX_{pPv})}{S_{Fe}} , \qquad (S8)$$

where S_T, S_{Fe}, and S_{pPv} are the sensitivities of V_S to temperature, iron, and pPv (see main text and Figure S5). Equation (S8) further requires the prescription of the anomaly in pPv, dX_{pPv}, which we fixed, again, from Figure S10d. Knowledge of iron anomalies from Eq. (S8) and temperature anomalies from Q_S gives access to estimates of relative anomalies in density ($dln\rho$) and compressional-wave velocity ($dlnV_P$) following

$$dln\rho = R_T dT_Q + R_{Fe} dx_{Fe} + R_{pPv} dX_{pPv} , \qquad (S9)$$

and $$dlnV_P = P_T dT_Q + P_{Fe} dx_{Fe} + P_{pPv} dX_{pPv} , \qquad (S10)$$

where R_T, R_{Fe}, R_{pPv}, P_T, P_{Fe}, and P_{pPv} are sensitivities of density and compressional-wave speed to temperature, iron, and pPv. To estimate $dln\rho$ in the western tip of the Pacific LLSVPs, *i.e.* from WP models in the depth-range 2600-2891 km, we averaged out the sensitivities of density to temperature and iron obtained by Deschamps et al. (2012) in this depth-range 2600-2891 km, leading to $R_T = (-1.2 \pm 0.05) \times 10^{-5}$ K^{-1} and $R_{Fe} = (0.31 \pm 0.05)$, and we assumed that pPv is denser than bridgmanite by 1.5 % (Cobden et al., 2015). This leads to a density excess, compared to the mantle average, of about (0.6 ± 0.4) %, in agreement with recent estimates of the density excess in LLSVPs from Earth's solid tides (Lau et al., 2017). Similarly, to estimate $dlnV_P$ in the western tip of the Pacific LLSVPs, we used sensitivities of compressional-wave speed from Deschamps et al. (2012) averaged out in the depth range 2600-2891 km, which gives $P_T = (-1.3 \pm 0.1) \times 10^{-5}$ K^{-1} and $P_{Fe} = (-0.19 \pm 0.04)$, and we assumed that V_P is almost unsensitive to pPv (Cobden et al., 2015). With these values, the combination of a 3.0-4.5 % iron excess and a 400 K temperature anomaly leads to $dlnV_P = (-1.2 \pm 0.4)$ %. This is slightly higher, but comparable to and consistent with the anomalies observed by global models of compressional-wave velocity, around -0.5 to -1.0 %

(Houser et al, 2008; Moulik and Ekström, 2016). If, as suggested by probabilistic tomography, LLSVPs are further enriched in bridgmanite by ~ 10 %, and assuming a sensitivity of V_P to bridgmanite $P_{Bm} = (0.06 \pm 0.04)$ (Deschamps et al., 2012), $dlnV_P$ gets closer to the global tomography values, around -0.6 %.

One may point out that a 1-2 km depression in CMB topography, as is expected if LLSVPs are associated with thermo-chemical piles (Deschamps et al., 2018), would result in delaying *ScS*, explaining, in turn, part of the observed shear-wave velocity anomaly. However, the region we explore is located close to the edge of the Pacific LLSVP. In that case, and according to numerical simulations (Deschamps et al., 2018), it may be located on the flanks of the depression caused by the Pacific LLSVP, *i.e.* the depression in the CMB at this specific location may be more limited than in the central regions of the LLSVP. By contrast, assuming that LLSVPs are purely thermal, and thus related to hot plumes, the CMB should be deflected upward. *ScS* phases would then be slightly in advance, implying that the observed $dlnV_S$ would underestimate the local anomaly. As a consequence, the temperature excess would be larger than the one we estimated, and thus even more difficult to reconcile with the temperature anomalies estimated from the quality factor. Finally, it is important to note that at the frequency range we use, 0.005-0.08 Hz, $dlnV_S$ are expected to be only slightly affected by changes in the CMB topography.

References

Cobden, L.J., Mosca, I., Trampert, J., Ritsema, J. 2012. On the likelihood of post-perovskite near the core-mantle boundary: A statistical interpretation of seismic observations. Phys. Earth Planet. Inter. 210, 21-35.

Cobden, L.J., Thomas, C., Trampert, J. 2015. Seismic detection of post-perovskite inside the Earth. In: Khan, A., and Deschamps, F. (Eds), The Earth's heterogeneous mantle, Springer, pp 391-440, doi:10.1007/978-3-319-15627-9_13.

Dannberg, J., Eilon, Z., Faul, U., Gassmöller, R, Moulik, P., Myhill, R., 2017. The importance of grain size to mantle dynamics and seismological observations. Geochem. Geophys. Geosys. 18, 3034-3061, doi: 10.1002/2017GC006944.

Deschamps, F., Kaminski, E., Tackley, P.J. 2011. A deep mantle origin for the primitive signature of ocean island basalt. Nature Geoscience 4, 879-882.

Deschamps, F., Cobden, L., Tackley, P.J., 2012. The primitive nature of large low shear-wave velocity provinces. Earth Planet. Sci. Lett. 349-350, 198-208.

Deschamps, F., Rogister, Y., Tackley, P.J., 2018. Constraints on core-mantle boundary topography from models of thermal and thermo-chemical convection. Geophys. J. Int. 212, 164-188.

Durek, J.J., Ekström, G., 1996. A radial model of anelasticity consistent with long-period surface wave-attenuation. Bull. Seismol. Soc. Am. 86, 144.158.

Dziewonski, A.M., Anderson, D.L., 1981. Preliminary Reference Earth Model. Phys. Earth Planet. Inter. 25, 297-356.

Fuji, N., Kawai, K., Geller, R.J., 2010. A methodology for inversion of broadband seismic waveforms for elastic and anelastic structure and its application to the mantle transition zone beneath the northwestern pacific. Phys. Earth planet. Inter. 180, 118–137.

Geller, R.J., Hara, T., 1993. Two efficient algorithms for iterative linearized inversion of seismic waveform data. Geophys. J. Int. 115, 699–710.

Getting, I.C., Dutton, S.J., Burnlay, P.C., Karato, S.-I., Spetzler, H.A., 1997. Shear attenuation and dispersion in MgO. Phys. Earth Planet. Inter. 99, 249-257.

Holzapfel, C., Rubie, D.C., Mackwell, S., Frost, D.J., 2003. Effect of pressure on Fe-Mg interdiffusion in $(Fe_xMg_{1-x})O$, ferropericlase. Phys. Earth Planet. Inter. 139, 21-34.

Holzapfel, C., Rubie, D.C., Frost, D.J., Langenhorst, F., 2005. Fe-Mg interdiffusion in $(Fe,Mg)SiO_3$ perovskite and lower mantle reequilibration. Science 309, 1707-1710.

Houser, C., 2007. Constraints on the presence or absence of post-perovskite in the lowermost mantle from long-period seismology. In: Hirose, K. et al. (Eds), Post-perovskite: the last mantle phase transition, Geophysical Monograph Ser. 174, American Geophysical Union, Washington DC, pp 191-216.

Houser, C., Masters, G., Shearer, P., Laske, G., 2008. Shear and compressional velocity models of the mantle from cluster analysis of long-period waveforms, Geophys. J. Int. 174, 195-212.

Jackson, I., Faul, U.H., 2010. Grainsize-sensitive viscoelastic relaxation in olivine: towards a robust laboratory-based model for seismological application. Phys. Earth Planet. Inter. 183, 151-163.

Konishi, K., Kawai, K., Geller, R.J., Fuji, N., 2014. Waveform inversion for localized three-dimensional seismic velocity structure in the lowermost mantle beneath the Western Pacific. Geophys. J. Int. 199, 1245-1267.

Konishi, K., Fuji, N., Deschamps, F., 2017. Elastic and anelastic structure of the lowermost mantle beneath the Western Pacific from waveform inversion. Geophys. J. Int. 208, 1290-1304.

Lau, H.C.P., Mitrovica, J.X., Davis, J.L., Tromp, J., Yang, H.-Y., Al-Attar, D., 2017. Tidal tomography constraints Earth's deep mantle buoyancy. Nature 551, 321-326.

Lau, H.C.P., Faul, U.H., 2019. Anelasticity from seismic to tidal timescales: theory and observations. Earth Planet. Sci. Lett. 508, 18-29.

Mao, W.L., Mao, H.-K., Sturhahn, W., Zhao, J., Prakapenka, V.B., Meng, Y., Shu, J., Fei, Y., Hemley, R.J., 2006. Iron-rich post-perovskite and the origin of ultralow-velocity zones, Science 312, 564–565.

Matas, J., Bukowinski, M.S.T., 2007. On the anelastic contribution to the temperature dependence of lower mantle seismic velocities. Earth Planet. Sci. Lett. 259, 51-65.

Mosca, I., Cobden, L., Deuss, A., Ritsema, J., Trampert, J., 2012. Seismic and mineralogical structures of the lower mantle from probabilistic tomography. J. Geophys. Res. 117, doi: 10.1029/2011JB008851.

Moulik, P., Ekström, G., 2016. The relationships between large-scale variations in shear velocity, density, and compressional velocity in the Earth's mantle, J. Geophys. Res. 121, 2737-2771.

Tackley, P.J., 2012. Dynamics and evolution of the deep mantle resulting from thermal, chemical, phase and melting effects. Earth Sci. Rev. 110, 1-25.

Trampert, J., Deschamps, F., Resovsky, J.S., Yuen, D.A., 2004. Probabilistic tomography maps significant chemical heterogeneities in the lower mantle. Science 306, 853-856.

Vallée, M., Charléty, J., Ferreira, A.M.G., Delouis, B., Vergoz, J., 2011. SCARDEC: a new technique for the rapid determination of seismic moment magnitude, focal mechanism and source time functions for large earthquakes using body wave deconvolution, Geophys. J. Int. 184, 338-358.

Yamazaki, D., Kato, T., Yurimoto, H., Ohtani, E., Toriumi, M., 2000. Silicon self-diffusion in $MgSiO_3$ perovskite at 25 GPa. Phys. Earth Planet. Inter. 119, 299-309.

Yamazaki, D., Irifune, T., 2003. Mg-Fe interdiffusion in magnesiowüstite up to 35 GPa. Earth Planet. Sci. Lett. 216, 301-311.

Supplementary Tables and Figures

Event #	Date (Y/M/D)	Latitude	Longitude	Depth	M_W	Global CMT id
1	2002 January 2	-17.63	178.84	680.8	6.1	010202E
2	2004 January 11	-16.27	-176.05	381.4	5.9	011104B
3	2000 May 4	-17.72	-178.31	539.8	6.4	050400K
4	2003 May 19	-18.02	-178.42	578.5	5.9	051903B
5	2002 June 16	-17.65	-178.5	588.1	5.9	061602C
6	2002 August 9	-16.25	-175.85	381.3	6.1	080902B
7	2003 October 15	-17.84	-178.59	594.9	5.9	101503A
8	2002 October 17	-19.8	-178.23	621.9	6.1	101702C
9	2001 November 5	-17.12	-178.96	579.7	6.2	110501D
10	2002 December 28	-18.0	-178.4	635.5	5.8	122802A
11	2006 February 24	-17.94	-179.42	640.9	6.1	200602241415A
12	2006 June 9	-17.36	-178.62	585.9	6.1	200606090558A
13	2006 July 23	-17.97	-178.42	597.9	5.8	200607232050A
14	2007 March 23	-18.87	-178.24	644.6	5.8	200703232230A
15	2007 April 9	-20.0	-177.97	613.7	5.9	200704090224A
16	2007 May 6	-19.44	-179.04	690.8	6.5	200705062111A
17	2007 May 6	-19.31	-179.05	691.6	6.0	200705062201A
18	2007 May 13	-19.58	-179.03	694.9	5.8	200705131126A
19	2008 April 18	-17.26	-178.98	577.8	6.3	200804182039A
20	2008 June 15	-17.77	-179.66	623.6	5.9	200806150113A
21	2008 December 17	-17.77	-178.3	547.8	5.8	200812171055A
22	2009 January 26	-17.83	-178.55	616.5	5.8	200901261154A
23	2009 January 27	-17.81	-178.51	612.7	5.9	200901270629A
24	2009 March 5	-17.46	-178.9	553.3	5.9	200903051933A
25	2009 November 22	-17.72	-178.36	546.4	6.3	200911220748A
26	2010 June 22	-19.16	-177.49	587.4	5.8	201006222216A
27	2011 April 3	-17.65	-178.45	562.3	6.4	201104031407A
28	2011 August 19	-16.52	-176.73	415.0	6.2	201108190354A
29	2011 October 27	-17.98	-179.4	608.7	6.0	201110270015A
30	2012 February 10	-17.98	-178.42	598.0	5.9	201202100147A
31	2013 November 23	-17.09	-176.38	386.6	6.5	201311230748A

Table S1 │ **List of events** used to build Western Pacific profiles.

Event #	Date (Y/M/D)	Latitude	Longitude	Depth	M_W	Global CMT id
1	2006 March 28	31.72	137.79	411.6	5.9	200603281332A
2	2008 July 20	27.81	139.60	485.6	5.8	200807202130A
3	2010 March 08	19.26	144.67	432.2	6.1	201003080947A
4	2010 November 30	28.69	139.26	460.6	6.8	201011300324A
5	2011 January 12	26.94	139.94	511.5	6.5	201101122132A
6	2011 October 04	26.73	140.35	439.6	5.7	201110040137A
7	2012 January 01	31.61	138.17	352.0	6.8	201201010527A
8	2012 May 26	26.87	140.17	472.1	6.0	201205262148A
9	2012 November 12	29.79	137.91	506.0	5.7	201211121115A
10	2013 May 14	18.67	145.35	604.7	6.8	201305140032A
11	2014 June 30	28.42	138.75	522.9	6.2	201406301955A

Table S2 │ List of events used to build Northern Pacific profiles.
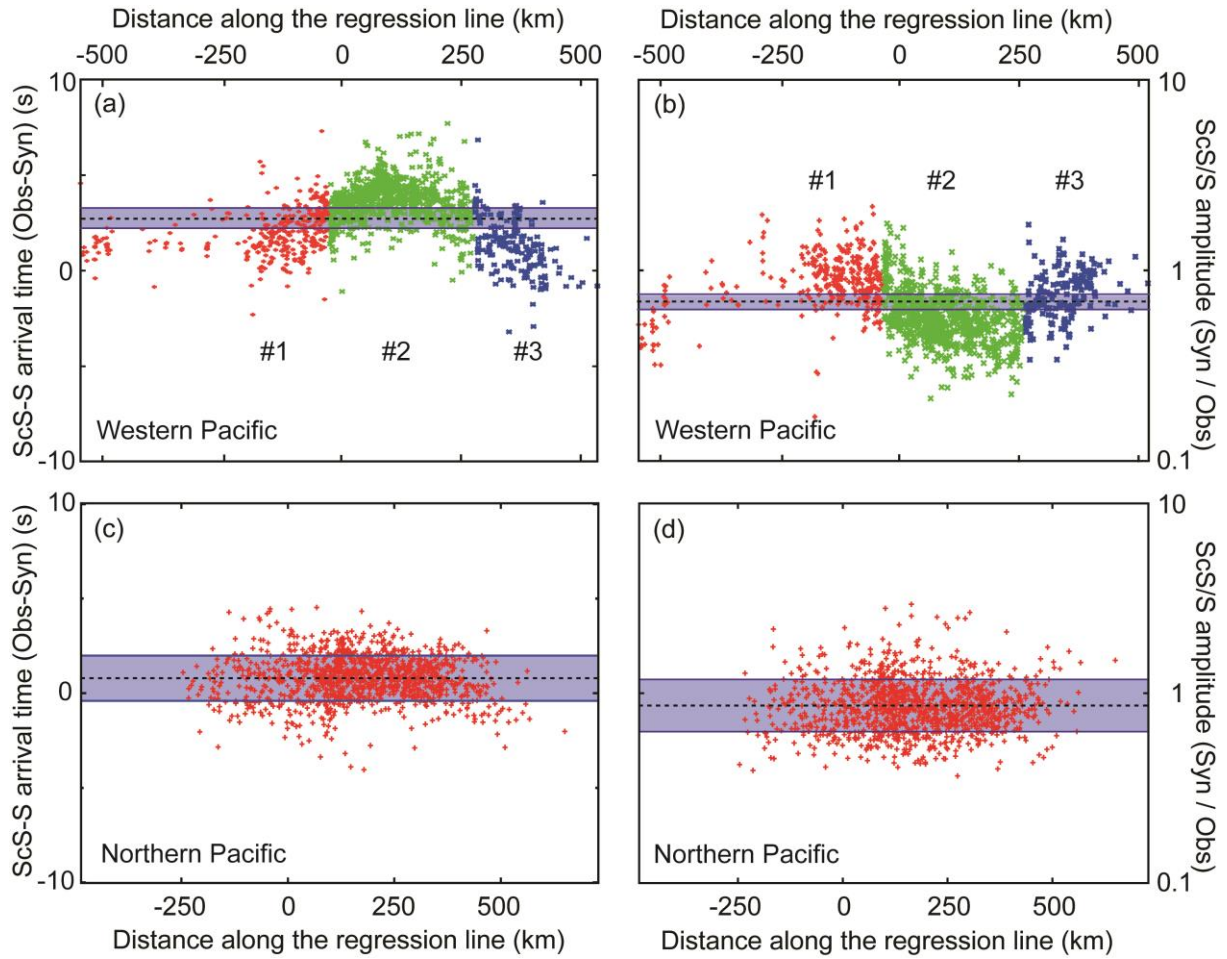
Figure S1 │ Traveltime residuals and amplitude ratios for the Western Pacific (WP, top row) and North Pacific (NP, bottom row) datasets. Each point represents a trace of the dataset projected on the regression line, *i.e.*, the line defined as the linear regression of all the bounce points of the raypaths on the CMB. (a and c) traveltime residuals. (b and d) amplitude ratios. The horizontal dashed lines and coloured bands denote the averages and standard deviations in travel time residuals and amplitude ratios over each dataset.
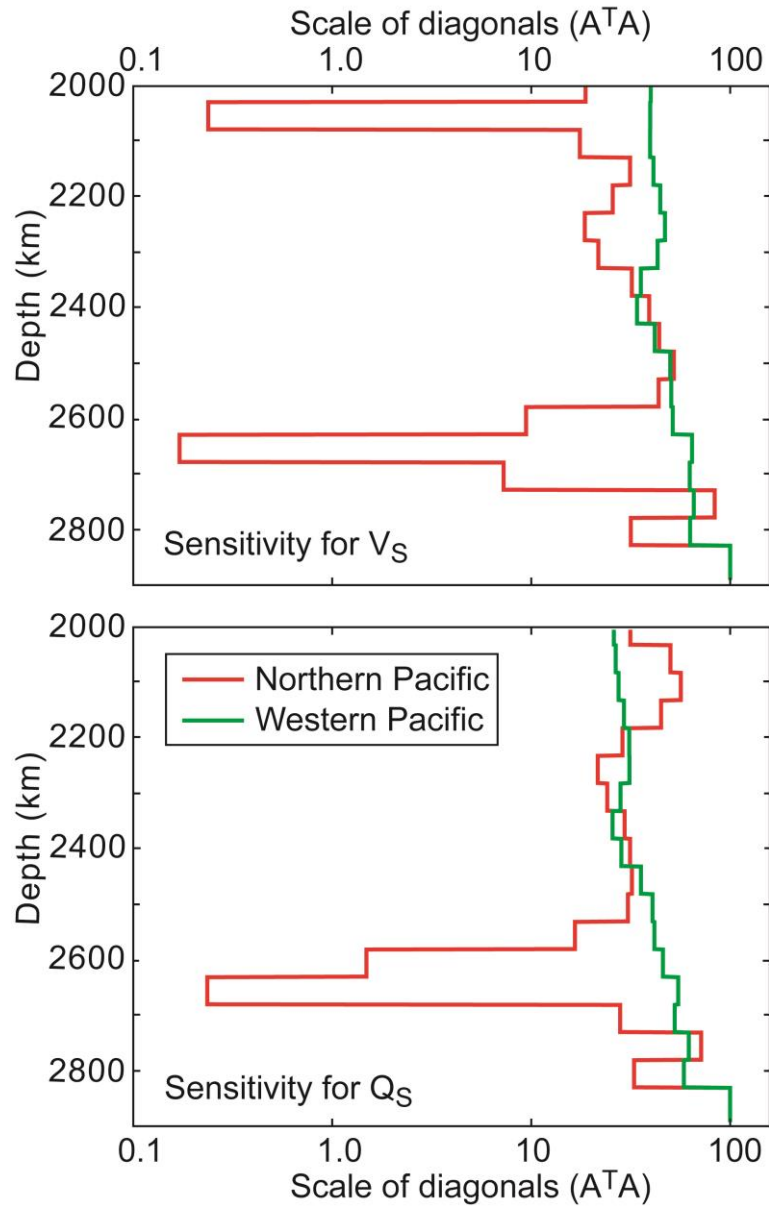
Figure S2 │ Depth sensitivity kernels for shear-wave speed (V_S, top) and quality factor (Q_S, bottom) in Western Pacific (green curves) and Northern Pacific (red curves) regions.
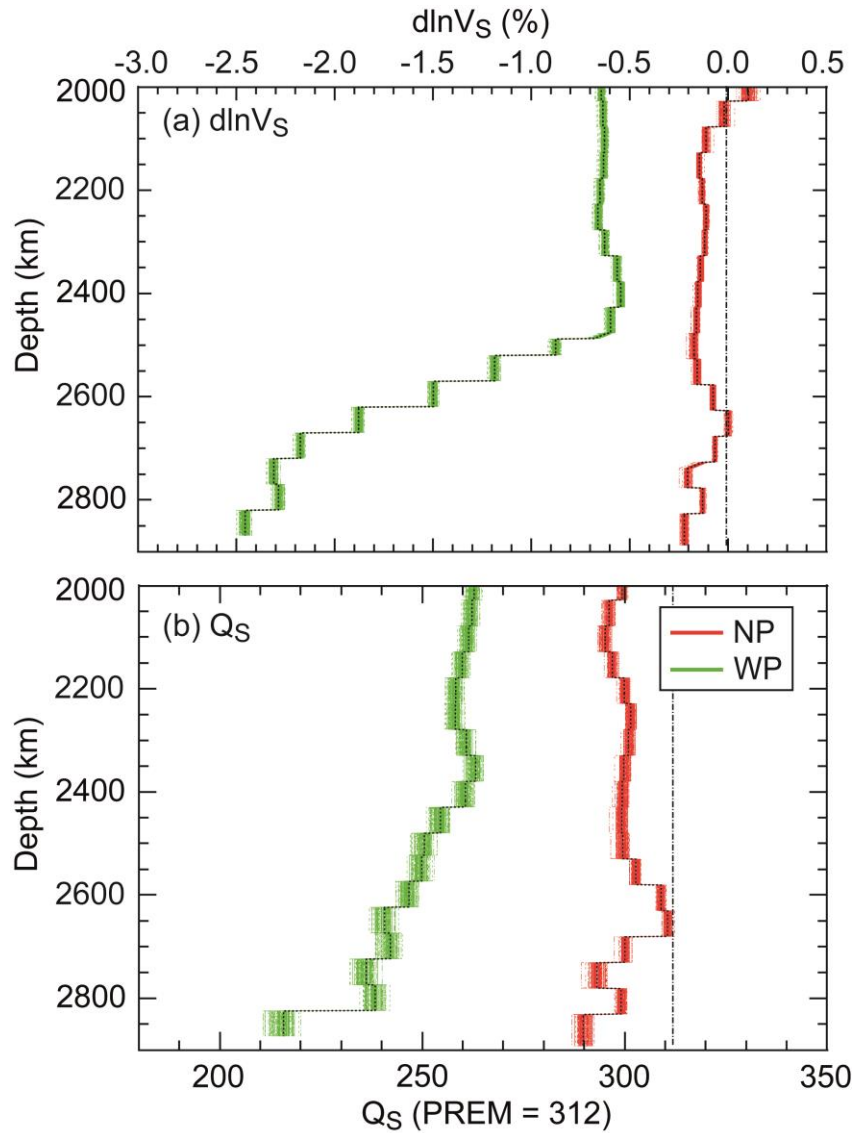
Figure S3 │ Bootstrap tests at Northern Pacific (NP, red curves) and Western Pacific (WP, green curves) locations. (a) Shear-wave velocity anomalies. (b) Quality factor. Each coloured curve represent a perturbed model (compared to our radial models) obtained by inverting 50 % of the waveforms in original datasets, all other parameters being similar to our radial models. Selected waveforms are randomly chosen, and we calculated a total of 100 perturbed curves. For comparison, the black dashed curves represent the models obtained with full datasets (Figure 3).
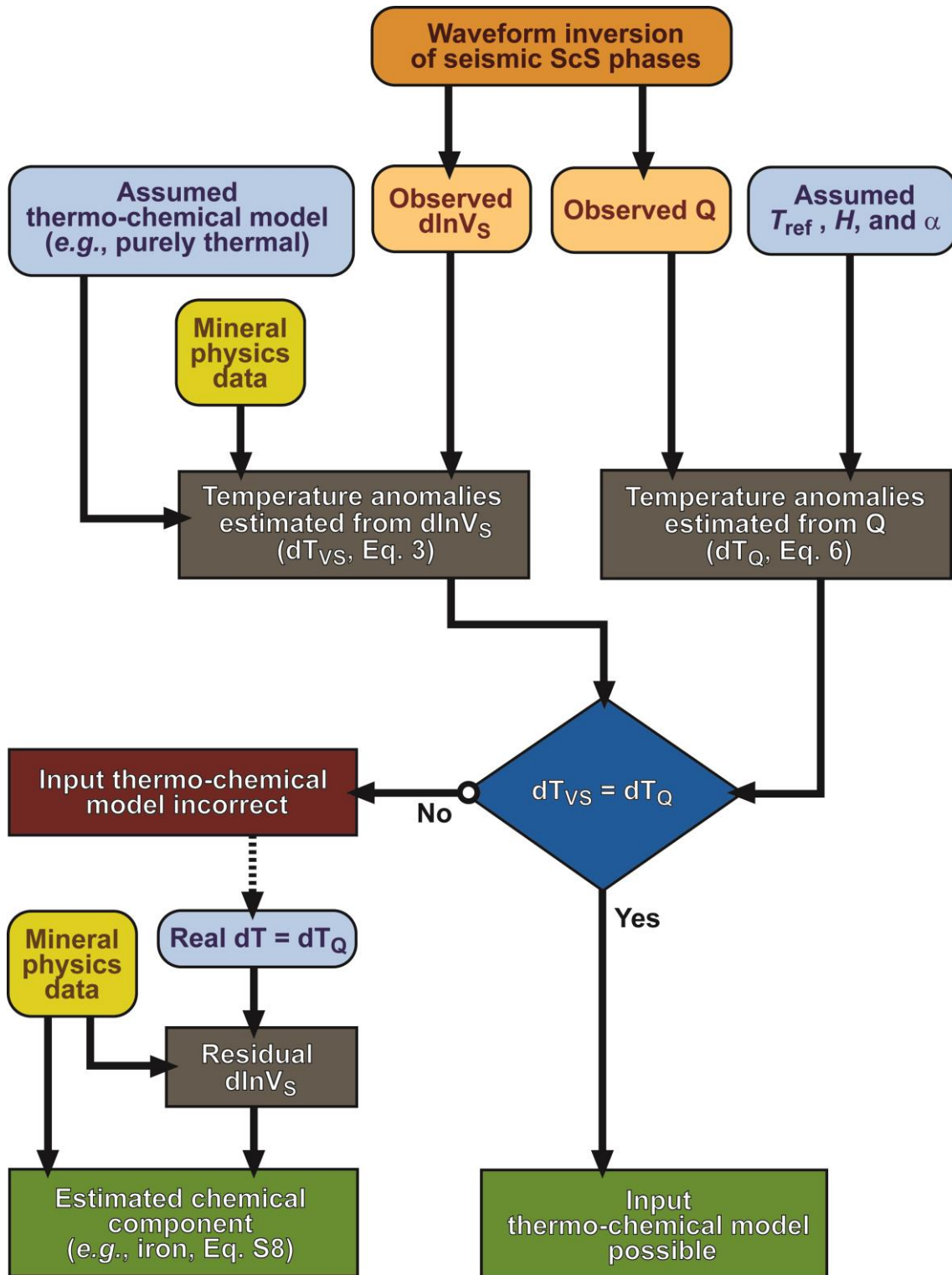
Figure S4 │ Flow chart summarizing our study. The same procedure is applied at both Western Pacific and Northern Pacific locations.
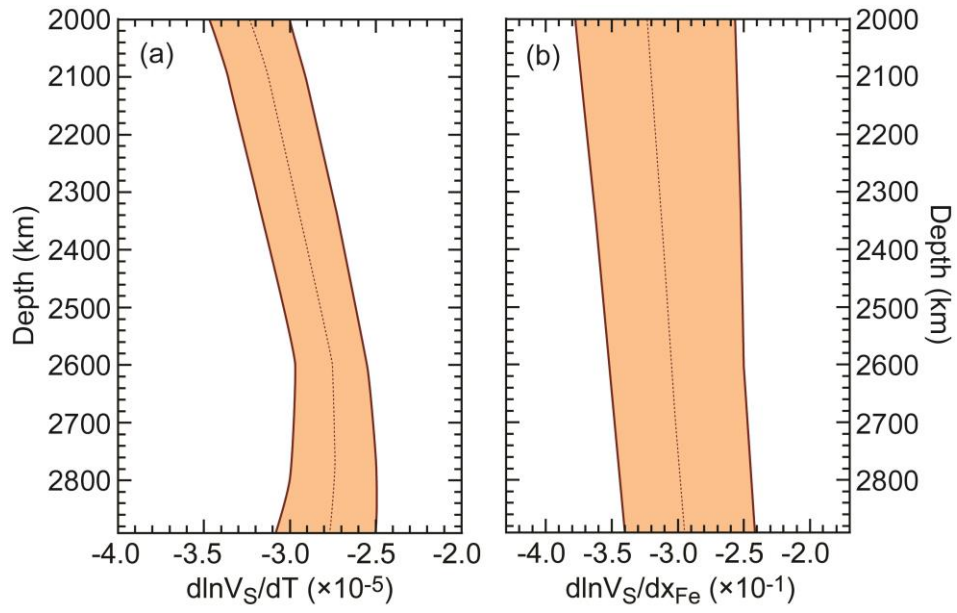
Figure S5 │ Sensitivities of shear-wave speed to temperature (left) and iron (right). Sensitivities are taken from Deschamps et al. (2012) and are plotted in the depth range $2000 \leq z \leq 2891$ km.
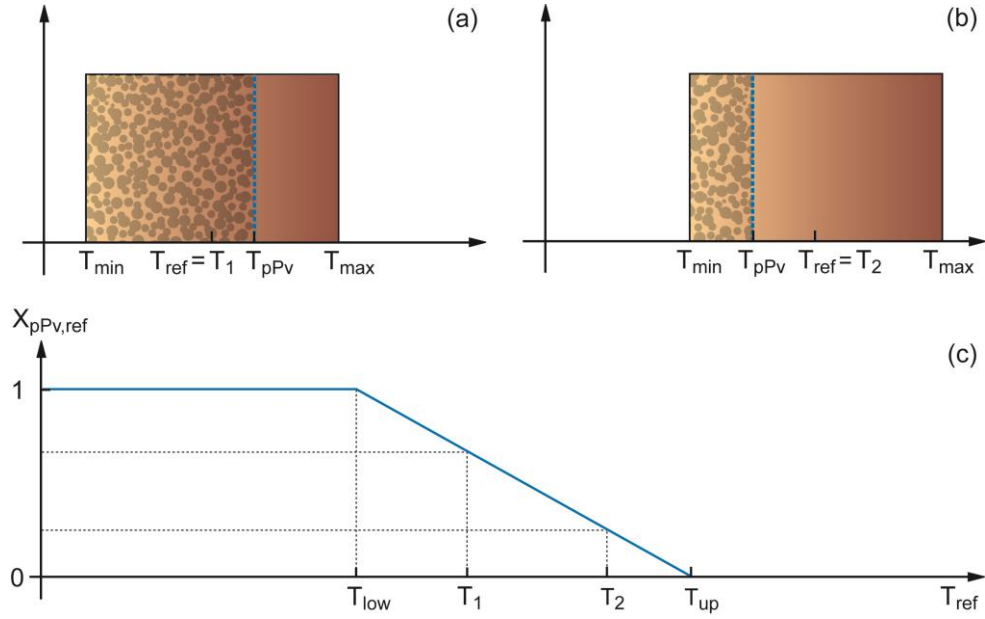
Figure S6 │ Calculation of the reference fraction of post-perovskite, $X_{pPv,ref}$ as a function of the reference temperature, T_{ref}. At a given depth, mantle temperature distribution is assumed to be entirely contained between $T_{min} = (T_{ref} - dT_{max})$ and $T_{max} = (T_{ref} + dT_{max})$ following a boxcar function (brown colored area in plots a and b), while the post-perovskite phase is stable at temperature lower than T_{pPv} (textured area in plots a and b). This implies that the average fraction of post-perovskite, $X_{pPv,ref}$, varies according to Eq. (S5), *i.e.* $X_{pPv,ref}$ is equal to 1 for $T_{ref} \leq T_{low} = (T_{pPv} - dT_{max})$, 0 for $T_{ref} \geq T_{up} = (T_{pPv} + dT_{max})$, and varies linearly between 1 and 0 for $T_{low} \leq T_{ref} \leq T_{up}$.
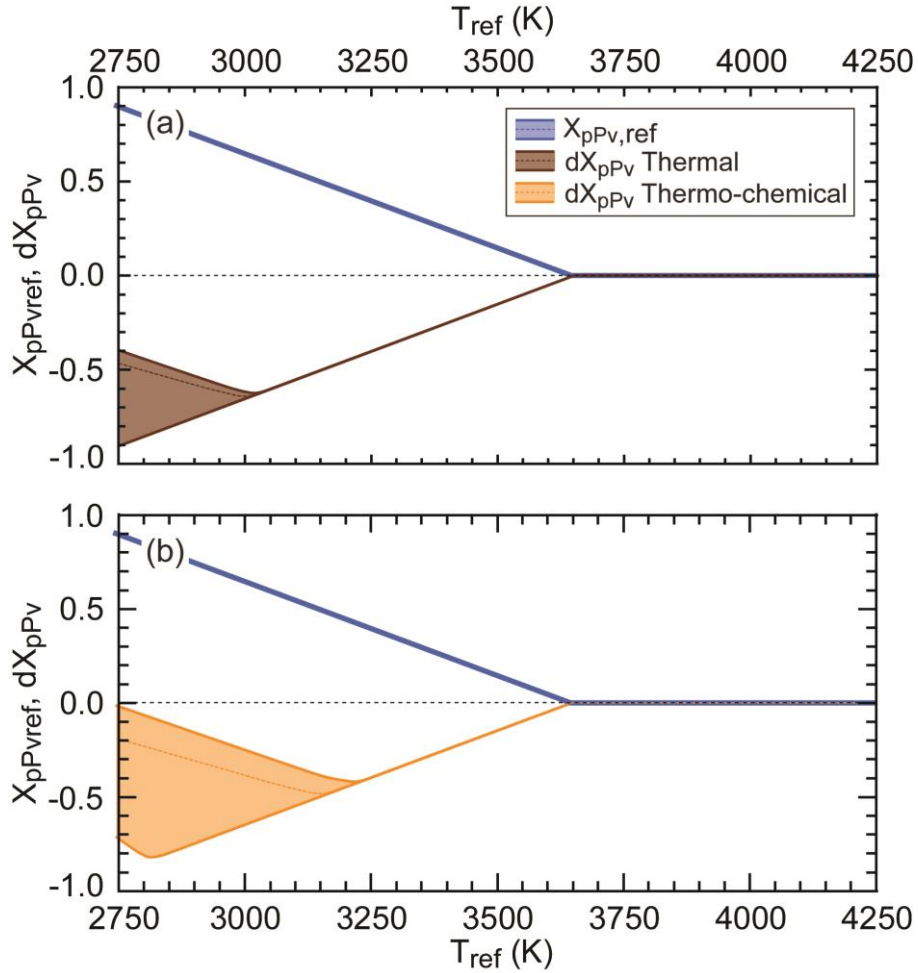
Figure S7 │ Anomalies in post-perovskite (dX_{pPv}) predicted by seismic velocity anomaly at WP as a function of the reference temperature, T_{ref}. Anomalies are calculated from anomalies in temperature dT_{VS} given by Eq. (3), and by substracting the reference fraction in post-perovskite (Eq. S5) from the local fraction of post-perovskite (Eq. S6). Two possible origin are tested: (a) purely thermal; and (b) thermo-chemical, assuming an enrichment in iron of 3.5 % at WP. Coloured dashed curves indicate the mean dX_{pPv} obtained for mean values of seismic sensitivities and observed dlnV_S, and the shaded areas shows uncertainties related to uncertainties in these parameters. The thick blue line represent the reference fraction of post-perovskite predicted by Eq. (S5).
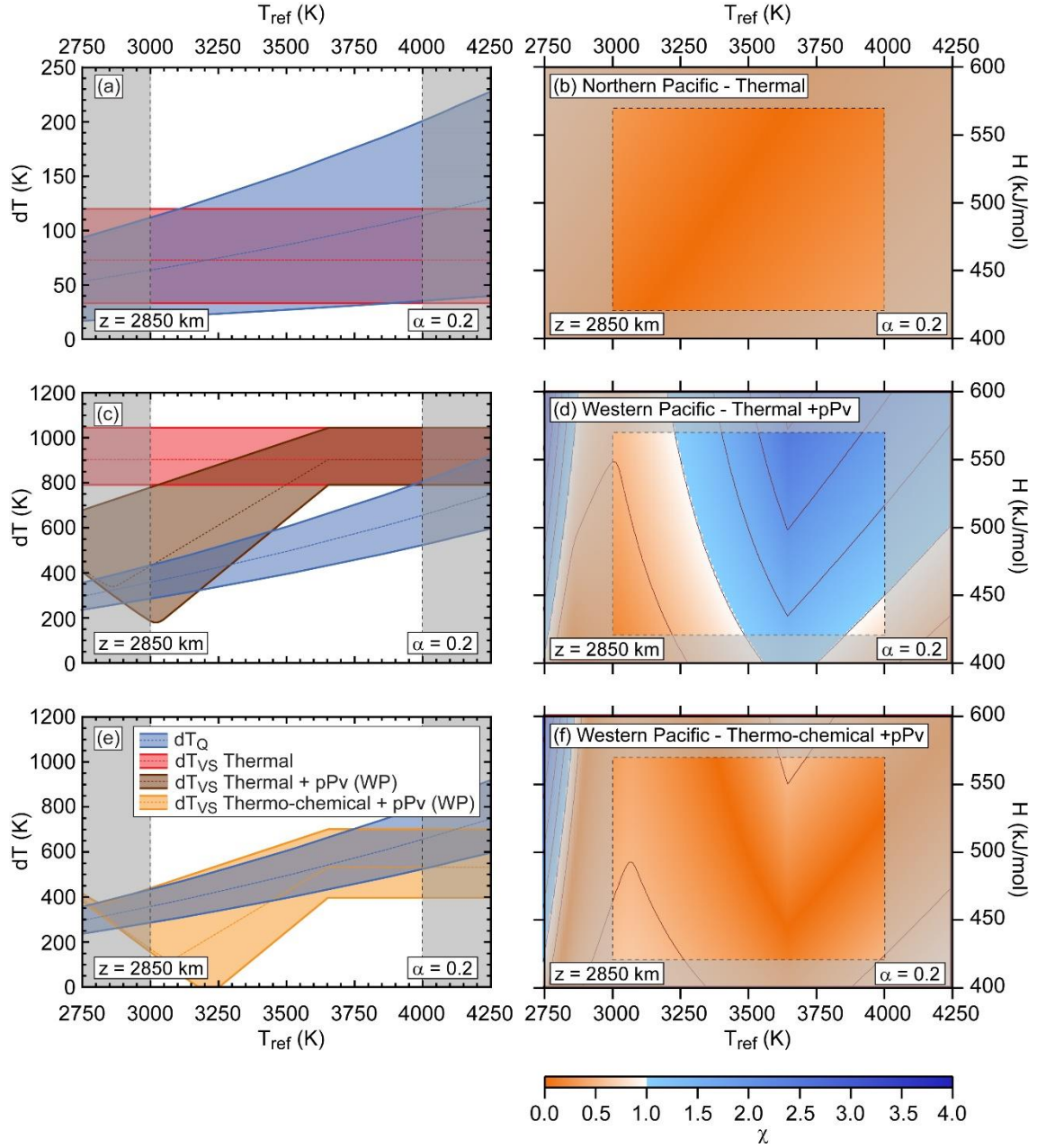
Figure S8 | Left column: temperature anomalies derived from seismic attenuation (dT_Q, Eq. 6) and shear-wave velocity (dT_{VS}, Eq. 3) as a function of reference temperature (T_{ref}). For each case, dotted curves and coloured areas represent the average and uncertainties in dT_Q and dT_{VS}. Right column: misfit function between and dT_Q and dT_{VS} (χ, Eq. 7) as a function of T_{ref} and activation enthalpy (H). Values of χ larger than 1 indicate that dT_Q and dT_{VS} disagree within their error bars. Locations are Northern Pacific (NP, plots a and b), and Western Pacific (plots c to f). At NP, shear-wave velocity anomalies are assumed to have a purely thermal origin. At WP, three possible origin are tested: purely thermal with or without post-perovskite (plots c and d), and thermo-chemical with post-perovskite (plots e and f). All calculations are made at $z = 2850$ km and for a frequency exponent $\alpha = 0.2$. Grey shaded areas indicate the ranges of T_{ref} and H that may be excluded (see main text and Supplementary Material).
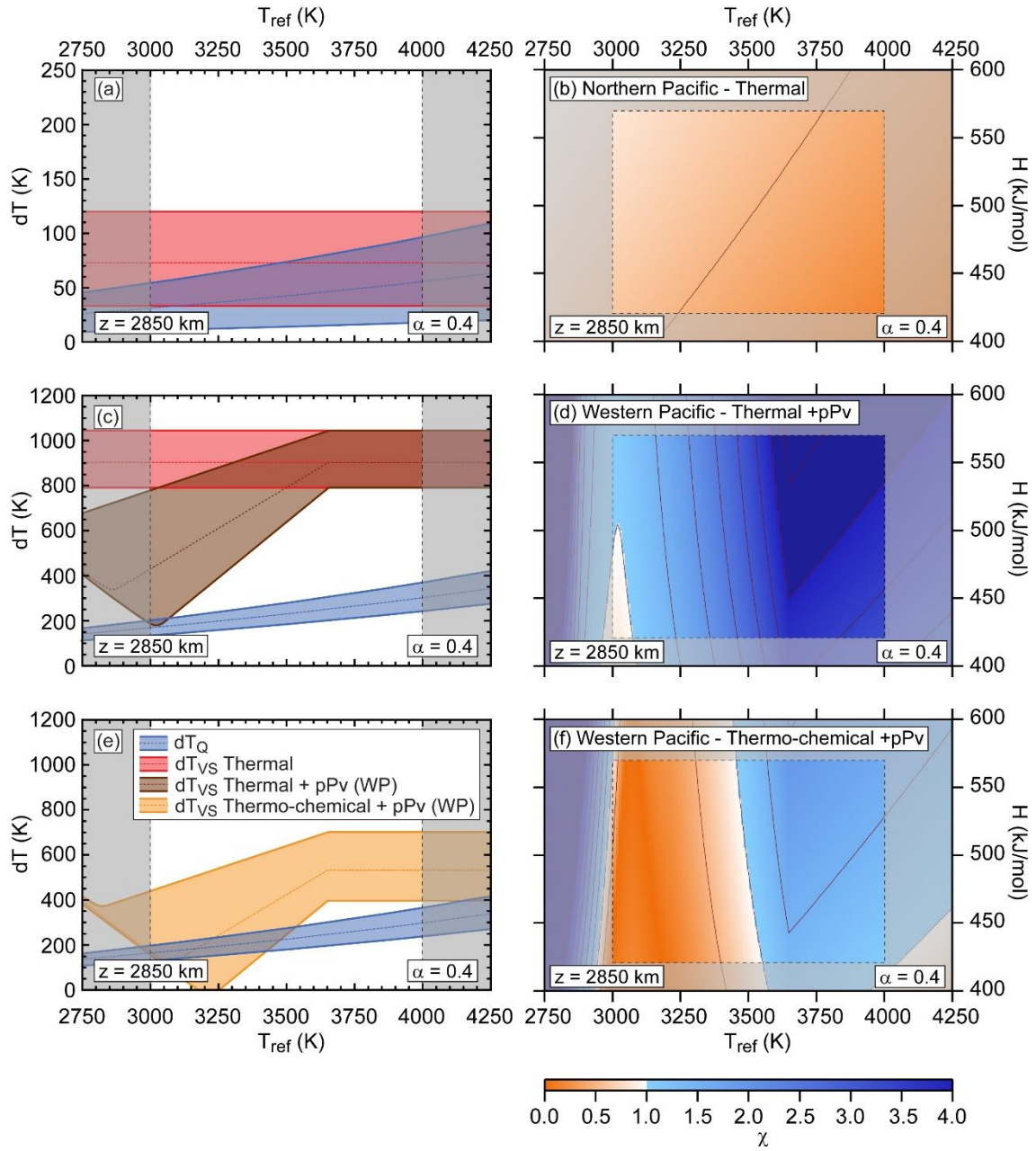
Figure S9 │ Same as Figures 6 and S8, but for α = 0.4.
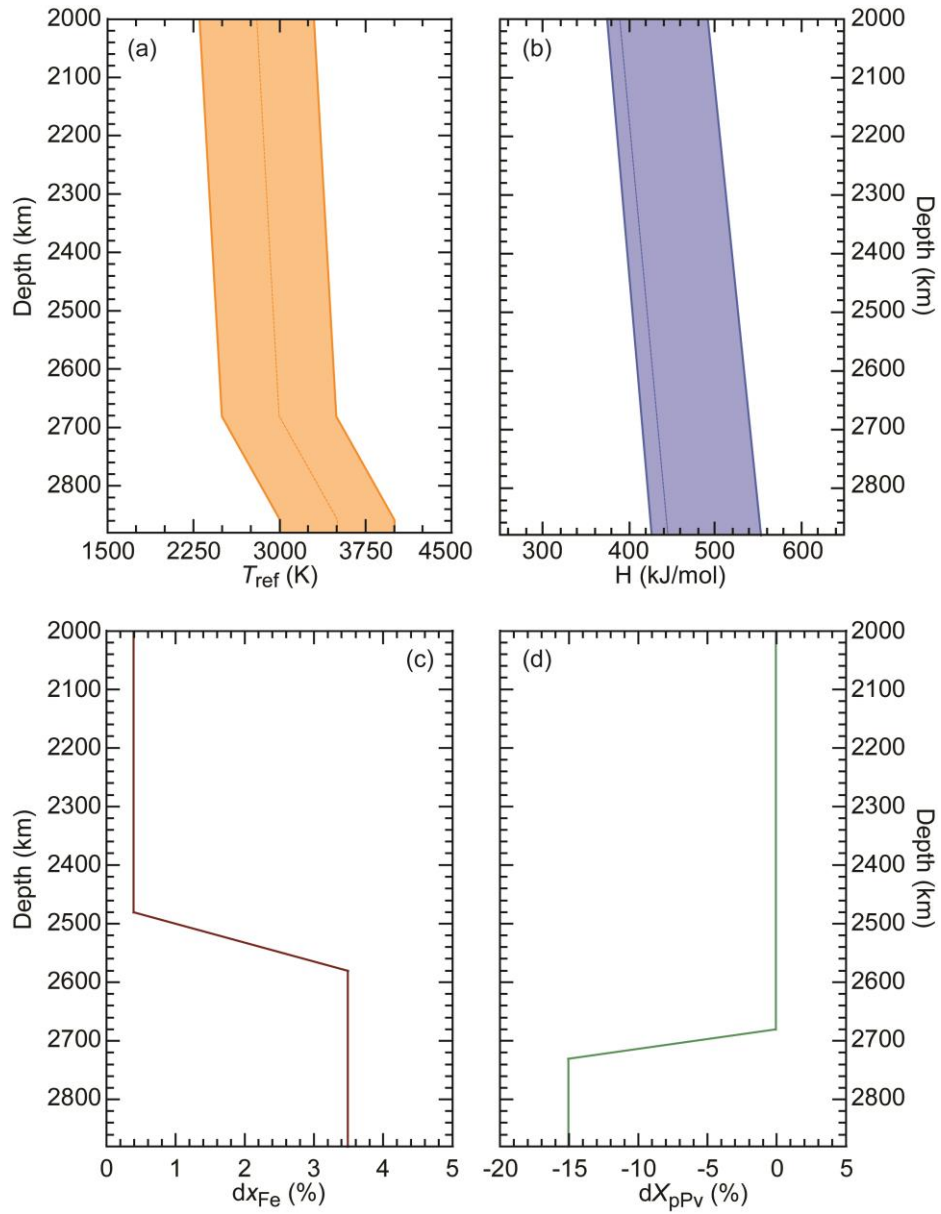
Figure S10 │ Depth variations of attenuation model parameters and *a priori* compositional model used to calculate models of temperature anomalies in Figures 8a and 8b. (a) Reference temperature, T_{ref}. (b) Activation enthalpy of quality factor, *H*. (c) Anomaly in iron oxide fraction, dx_{Fe}. (d) Anomaly in post-perovskite fraction, dX_{pPv}.